

Continuum Halos in Nearby Galaxies – an EVLA Survey (CHANG-ES) – II: First Results on NGC 4631

Judith Irwin¹, Rainer Beck², R. A. Benjamin³, Ralf-Jürgen Dettmar⁴, Jayanne English⁵,
George Heald⁶, Richard N. Henriksen⁷, Megan Johnson⁸, Marita Krause⁹, Jiang-Tao Li¹⁰,
Arpad Miskolczi¹¹, Silvia Carolina Mora¹², E. J. Murphy¹³, Tom Oosterloo¹⁴,
Troy A. Porter¹⁵, Richard J. Rand¹⁶, D. J. Saikia¹⁷, Philip Schmidt¹⁸,
A. W. Strong¹⁹, Rene Walterbos²⁰, Q. Daniel Wang²¹
and

Theresa Wiegert²²

ABSTRACT

We present the first results from the CHANG-ES survey, a new survey of 35 edge-on galaxies to search for both in-disk as well as extra-planar radio continuum emission. CHANG-ES is exploiting the new wide-band, multi-channel capabilities of the Karl G. Jansky Very Large Array (i.e. the Expanded Very Large Array, or EVLA) with observations in two bands centered at 1.5 and 6 GHz in a variety of array configurations with full polarization. The motivation and science case for the survey are presented in a companion paper (Paper I). These first results are based on C-array test observations in both observing bands of the well-known radio halo galaxy, NGC 4631. In this paper, we outline the observations and the data reduction steps that are required for wide-band calibration and mapping of EVLA data, including polarization.

With modest on-source observing times (30 minutes at 1.5 GHz and 75 minutes at 6 GHz for the test data) we have achieved best rms noise levels of 22 and $3.5 \mu\text{Jy beam}^{-1}$ at 1.5 GHz and 6 GHz, respectively. New disk-halo features have been detected, among them two at 1.5 GHz that appear as loops in projection.

We present the first 1.5 GHz spectral index map of NGC 4631 to be formed from a single wide-band observation in a single array configuration. This map represents tangent slopes to the intensities within the band centered at 1.5 GHz, rather than fits across widely separated frequencies as has been done in the past and is also the highest spatial resolution spectral index map yet presented for this galaxy. The average spectral index in the disk is $\bar{\alpha}_{1.5\text{GHz}} = -0.84 \pm 0.05$ indicating that the emission is largely non-thermal, but a small global thermal contribution is sufficient to explain a positive curvature term in the spectral index over the band. Two specific star forming regions have spectral indices that are consistent with thermal emission.

Polarization results (uncorrected for internal Faraday rotation) are consistent with previous observations and also reveal some new features. On broad scales, we find strong support for the notion that magnetic fields constrain the X-ray emitting hot gas.

Subject headings: ISM: bubbles – (ISM:) cosmic rays – ISM: magnetic fields – galaxies: individual (NGC 4631) – galaxies: magnetic fields – radio continuum: galaxies

¹Dept. of Physics, Engineering Physics & Astronomy,
Queen's University, Kingston, ON, Canada, K7L 3N6,

²irwin@astro.queensu.ca.

²Max-Planck-Institut

für

Radioastronomie,

Auf dem Hügel 69, 53121, Bonn, Germany,
rbeck@mpifr-bonn.mpg.de.

³Dept. of Physics, University of Wisconsin at Whitewater, 800 West Main St., Whitewater, WI, USA, 53190, benjamin@wisp.physics.wisc.edu.

⁴Astronomisches Institut, Ruhr-Universität Bochum, 44780 Bochum, Germany, dettmar@astro.rub.de.

⁵Department of Physics and Astronomy, University of Manitoba, Winnipeg, Manitoba, Canada, R3T 2N2, jayanne_english@umanitoba.ca.

⁶Netherlands Institute for Radio Astronomy (ASTRON), Postbus 2, 7990 AA, Dwingeloo, The Netherlands, heald@astron.nl.

⁷Dept. of Physics, Engineering Physics & Astronomy, Queen's University, Kingston, ON, Canada, K7L 3N6, henriksn@astro.queensu.ca.

⁸National Radio Astronomy Observatory, P. O. Box 2, Greenbank, WV, USA, 24944, mjohnson@nrao.edu.

⁹Max-Planck-Institut für Radioastronomie, Auf dem Hügel 69, 53121, Bonn, Germany, mkrause@mpifr-bonn.mpg.de.

¹⁰Dept. of Astronomy, University of Massachusetts, 710 North Pleasant St., Amherst, MA, 01003, USA, jiangtao@astro.umass.edu.

¹¹Astronomisches Institut, Ruhr-Universität Bochum, 44780 Bochum, Germany, miskolczi@astro.rub.de.

¹²Max-Planck-Institut für Radioastronomie, Auf dem Hügel 69, 53121, Bonn, Germany, cmora@mpifr-bonn.mpg.de.

¹³Observatories of the Carnegie Institution for Science, 813 Santa Barbara Street, Pasadena, CA, 91101, USA, emurphy@obs.carnegiescience.edu.

¹⁴Netherlands Institute for Radio Astronomy (ASTRON), Postbus 2, 7990 AA, Dwingeloo, The Netherlands, oosterloo@astron.nl.

¹⁵Hansen Experimental Physics Laboratory, Stanford University, 452 Lomita Mall, Stanford, CA, 94305, USA, tporter@stanford.edu.

¹⁶Dept. of Physics and Astronomy, University of New Mexico, 800 Yale Boulevard, NE, Albuquerque, NM, 87131, USA, rjr@phys.unm.edu.

¹⁷National Centre for Radio Astrophysics, TIFR, Pune University Campus, Post Bag 3, Pune, 411 007, India, djs@ncra.tifr.res.in.

¹⁸Max-Planck-Institut für Radioastronomie, Auf dem Hügel 69, 53121, Bonn, Germany, pschmidt@mpifr-bonn.mpg.de.

¹⁹Max-Planck-Institut für extraterrestrische Physik, Garching bei München, Germany, aws@mpe.mpg.de.

²⁰Dept. of Astronomy, New Mexico State University, PO Box 30001, MSC 4500, Las Cruces, NM 88003, USA, rwalterb@nmsu.edu.

²¹Dept. of Astronomy, University of Massachusetts, 710 North Pleasant St., Amherst, MA, 01003, USA, wqd@astro.umass.edu.

²²Dept. of Physics, Engineering Physics & Astronomy,

1. Introduction

We present results of radio continuum observations of the edge-on galaxy, NGC 4631, using the Karl G. Jansky Very Large Array (hereafter, the Expanded Very Large Array, or EVLA) in its C configuration. These are the first results from a new survey, Continuum Halos in Nearby Galaxies – an EVLA Survey (CHANG-ES), whose motivation, science goals, galaxy sample criteria, and expectations for improvements over previous surveys are described in a companion paper (Irwin et al. 2012, hereafter, Paper I). The sample consists of 35 nearby edge-on galaxies and observations are being carried out in two frequency bands (1.5 GHz and 6 GHz, i.e. in L-band and C-band, respectively) in all polarization products. The survey includes observations in three EVLA array configurations (B, C, and D) but the test data presented here were obtained at both frequencies in the C configuration only.

In this second paper, our goals are to outline the observations and data reduction procedures used for the test data (Sect. 2) and to present the initial scientific results for NGC 4631 (Sect. 3). We pay particular attention to the data reduction procedures, especially with respect to differences that are introduced by using the wide EVLA frequency bands that are now available.

The galaxy, NGC 4631, was chosen because of its extensive radio continuum halo which has been known for some time (Ekers & Sancisi 1977). For a recent summary of previous observations of this galaxy, see Irwin et al. (2011). In this paper, we refer to the region, $0.2 \lesssim z \lesssim 1$ kpc, as the disk-halo interface and use ‘halo’ for emission on larger scales ($z \gtrsim 1$ kpc). ‘High-latitude’ or ‘extraplanar’ are also used to describe either of these components. It is worth keeping in mind that halos are not necessarily smooth since substructure is generally observed, depending on the spatial scales that are probed.

Queen's University, Kingston, ON, Canada, K7L 2T3, twiegert@astro.queensu.ca.

2. EVLA Observations of NGC 4631

2.1. Observations

Observations of NGC 4631 were carried out on 11 Nov. 2010 with the pointing center set to the center of the galaxy at RA = 12^h 42^m 08^s.01, DEC = 32° 32′ 29″.4. The observing set-up is summarized in Table 1. All EVLA observations (including continuum) are now done in spectral line mode which facilitates the excision of radio frequency interference (RFI) from the data, effectively enables broader uv coverage via multi-frequency synthesis techniques (Sect. 2.4) and permits the extraction of spectral index information (Sect. 2.6)¹.

At the time of the observations, the WIDAR correlator was restricted to a maximum of 8 spectral windows (spws) per base-band, i.e. per AC or BD intermediate frequency (IF). Each spectral window has its own bandpass response, and contains 64 channels. With AC and BD IFs contiguous in frequency, the result was 1024 spectral channels centered at 1.5 GHz (L-band) for a total bandpass of 512 MHz, and 1024 channels centered at 6.0 GHz (C-band) for a total bandpass of 2.048 GHz.

Clearly, at the lower frequency, the achievable bandwidth cannot be higher than the frequency itself, but the L-band bandwidth (more so than C-band) also suffers from RFI², restricting the bandwidth further. In fact, although we avoided known RFI at the ends of the band, we found that the L-band RFI, especially in the 1.52 to 1.64 GHz region within our band, to be persistent throughout our observations. Together with other flagging, this reduced the effective L-band bandwidth to approximately 300 MHz and has prompted a modification of the correlator set-up for subsequent observations. The strength of the RFI in L-band achieved a maximum value which was 300 times that of 3C286 (the flux calibrator) so that even the sidelobes of the RFI swamped that of our astronomical sources at some frequencies. Experimentation with flagged and unflagged data showed that it was not, in general, possible to salvage the long-spacing uv data while flagging

only the short-spacings; once RFI was detected, all uv data had to be removed over the time and frequency ranges that were affected. RFI at C-band was also present, but much less severe than in L-band.

Observations were carried out in the standard fashion, including scans of a flux calibrator (which was also used as a bandpass calibrator as well as for the determination of absolute polarization position angle), a ‘zero-polarization’ calibrator (to determine the instrumental polarization) and a phase calibrator. The flux calibrator was observed in 3 independent scans at each frequency for these test observations. Only a single scan is necessary, in principle, but these data were intentionally ‘over-calibrated’ for consistency checks. The zero-polarization calibrator was observed once at each frequency.

The L-band observation of NGC 4631 was carried out in a single time block containing one on-source scan flanked by phase calibrator scans (plus the flux and zero-polarization calibrator). The C-band observation of NGC 4631 with its calibrators was similarly observed in a single time block, but separated into 3 individual scans interspersed with phase calibrator scans. Observations at each frequency were carried out within single blocks of total observing time in order to minimize time spent on overheads. For the regular data, however, attempts are being made, where possible, to split the observing time for given galaxy at each frequency into two observing blocks that are widely separated in hour angle; more time is then spent on overheads but the result should be improved uv coverage with a better-behaved beam, as well as lower off-axis instrumental polarization (Sect. 2.3).

2.2. Total Intensity Calibration

The data were reduced using the Common Astronomy Software Applications (CASA) package³, unless otherwise indicated. As improvements to CASA are frequently being made during EVLA commissioning, a number of versions of CASA were employed in the data reductions, in particular versions that were extant over the period May 2011 to July 2011. The following steps were carried out for both the L-band and C-band data sep-

¹It will also allow an analysis of Faraday rotation, to be described in future papers; see Paper I for related science.

²A list of known RFI is given at <https://science.nrao.edu/facilities/evla/observing/rfi>.

³Available at <http://casa.nrao.edu>.

arately.

On-line Hanning smoothing is no longer an option at the EVLA, so all data were first Hanning smoothed to minimize Gibbs ringing in frequency, a step which significantly ameliorated RFI detection throughout the band. As a result, the frequency resolution is twice the channel width, the latter listed in Table 1⁴. A significant amount of time was then spent flagging RFI. Experimentation with automatic flagging routines had not yet provided results that were as dependable as manual flagging, requiring that flagging be done by hand; however, such routines are improving and should shorten the data reduction process in the future.

The flux density, I_ν , (Stokes I) of the flux calibrator, 3C 286, was first set for the frequency, ν , of each spectral window using a known model and the ‘Perley-Taylor-99’ calibration scale⁵. Since each spectral window of each antenna has its own bandpass response, bandpass calibrations were required, again using 3C 286. However, since the data are vector-averaged when producing an average bandpass for each spectral window, it is necessary to first carry out an initial gain and phase calibration with time; applying the solution ensures that phase variations that may occur over the different scans of 3C 286 when it is observed through different elevations do not result in decorrelation when vector-averaging occurs. With the initial gain/phase solutions applied, bandpasses were then determined, one for each spectral window of each antenna, and the initial gain and phase solution is no longer used.

The gain and phase were then calibrated with time for each of the flux, zero-polarization, and phase calibrators, where an antenna-based solution is found for each spectral window and each separate scan, followed by bootstrapping of the flux from the flux calibrator to both the zero-polarization (OQ 208) and phase (J1221+2813) calibrators for each spectral window. At L-band, the flux densities of OQ 208 and J1221+2813 varied systematically over the band from 0.72 to 1.16

Jy (positive spectral index⁶ with an error of about 0.3% on each spectral window value) and from 0.55 to 0.53 Jy (negative spectral index with an error of about 0.7% on each spectral window value), respectively. At C-band, the flux densities of the two calibrators (in the same order) varied from 2.4 to 1.9 Jy (negative spectral index with an error of about 0.4% on each spectral window value) and from 0.46 to 0.44 Jy (negative spectral index with an error of about 0.5% on each spectral window value), respectively. The changing spectral index of OQ 208 (positive in L-band and negative in C-band) is in good agreement with the known spectrum which peaks around 4 GHz (Cenacchi, Dallacasa, & Orfei 2006, or the Nasa Extragalactic Database).

The bandpass and gain/phase solutions as a function of time were then applied to all sources, antenna by antenna, and spectral window by spectral window, with the gain/phase solutions from the phase calibrator interpolated in time when applied to NGC 4631⁷.

2.3. Polarization Calibration

Polarized intensity, P, and the polarization angle on the sky, χ , require calibration of Stokes Q and U. To initially set Stokes Q and U for 3C 286, the absolute position angle on the sky is assumed to be constant at $\chi = 33$ deg, but the percentage polarization varies with frequency. We obtained detailed EVLA data on this calibrator (R. Perley, private communication) and fit a curve through the L-band data of the form,

$$P_\nu = -1.443 \times 10^{-6} \nu^2 + 0.006026 \nu + 3.858 \quad (1)$$

where P_ν is the percent polarization at frequency, ν (MHz). In C-band, only a linear fit was necessary,

$$P_\nu = 0.0001583 \nu + 10.57 \quad (2)$$

(ν in MHz). The estimated error, including measurement errors and fitted curves is of order 0.3%.

⁶ $S_\nu \propto \nu^\alpha$.

⁷In practice, application of the calibration tables revealed that more flagging for RFI was required, necessitating a second iteration through the calibration. The fluxes quoted in this section apply to the final iteration. At various stages in the data reduction, occasionally additional flagging of RFI was carried out. Wherever such flagging affected the calibration or imaging, the necessary steps were redone.

⁴If corrections are required for antenna position or antenna-based delays, they would be carried out prior to the Hanning smoothing step.

⁵See <http://www.vla.nrao.edu/astro/calib/manual/baars.html>.

Q and U were then calculated at the frequency of each spectral window via

$$Q_\nu = (P_\nu/100) * I_\nu * \cos(2\chi) \quad (3)$$

$$U_\nu = (P_\nu/100) * I_\nu * \sin(2\chi) \quad (4)$$

where the total intensity, I_ν , has previously been set via a known model (Sect. 2.2).

There is leakage between the right circularly polarized (R) and left circularly polarized (L) feeds at the EVLA and this leakage must be determined in order to calibrate the cross-terms (RL, LR) from which Q and U are calculated⁸. The leakage terms (referred to as the ‘D’ terms) were determined from the ‘zero-polarization’ source, OQ 208⁹ after first applying the previously determined gain/phase and bandpass solutions.

Finally, the absolute polarization angle on the sky (the R-L phase difference) was calibrated from the known position angle of 3C 286, after first applying solutions for gain/phase, bandpass, and D terms.

All corrections were then applied to the calibrators and the source (gain/phase, bandpass, D terms, and absolute position angle corrections).

The polarization calibration described in this section corrects for ionospheric Faraday rotation, provided that this rotation is constant with time and position in the sky. As neither may be the case, it is important to determine the magnitude of such variations. At present, there is no CASA routine to do this, but there is (the task, TECOR) in the Astronomical Image Processing System (AIPS). We therefore copied a small amount of L-band data from each calibrator, ensuring that all observing times were represented in the copied data set, into AIPS for this purpose. (Corrections for the source are assumed to be the same as those for the phase calibrator, given their close proximity in the sky.) TECOR derives corrections for ionospheric Faraday rotation from maps of total electron content obtained from NASA’s crustal dynamics data interchange system (CCDIS¹⁰) which cover the time range of the observations. These measurements provide a crude correction since the spatial resolution is typically coarser than the source size. Therefore, if

⁸ $Q = (RL + LR)/2$, $U = (RL - LR)/2i$.

⁹<http://evlaguides.nrao.edu/index.php?title=Category:Polarimeter>

¹⁰<http://cddis.gsfc.nasa.gov/>

significant fluctuations exist on smaller scales, we cannot correct for them.

In L-band, we find that the differential ionospheric Faraday rotation ranges from a minimum of 2.365 to a maximum of 2.805 rad m⁻² over all sources, positions, and times. This result corresponds to a variation of 0.44 rad m⁻², or 0.74 deg at the high frequency end of the band and 1.45 deg at the low frequency end. Thus a typical error introduced by ignoring time variable or position variable ionospheric Faraday rotation is about 1 deg and we therefore have made no additional correction for Faraday rotation at L-band beyond the non-differential term that has already been taken into account in the normal data reduction. Moreover, since Faraday rotation $\propto \lambda^2$ and since the L-band and C-band observations were close together in time, no additional correction was necessary in C-band either.

Finally, the accuracy of wide field linear polarization imaging is limited by variations in instrumental polarization as a function of angle from the pointing center; that is, the corrections that have now been applied are accurate only for the on-axis position. The off-axis instrumental polarization for a ‘snapshot’ observation¹¹ is estimated to be less than a few percent within the half-power point of the primary beam¹² and increases at larger angles. In this paper, our polarization results (Sect. 3.2) are shown only over regions that are within the primary beam full width at half maximum (FWHM). In addition, when sources are tracked, the source parallactic angle rotates through the primary beam, minimizing the off-axis polarization errors. Hence for these data, this effect is negligible. Nevertheless, for future wide-field polarization mapping, a correction will likely be required; a CASA algorithm is currently being developed to aid in this process.

2.4. Imaging

Our goal is to form single I, Q, and U maps of NGC 4631 from each of the L-band and C-band data; maps of linear polarization intensity,

¹¹We take this to mean any observation short enough that Earth rotation does not fill in uv tracks.

¹²See the *Observational Status Summary* at <http://evlaguides.nrao.edu> or earlier references such as <http://www.vla.nrao.edu/astro/guides/vlas/current/node35.html> and Brisken (2003).

P, and magnetic field position angle, χ , can then be formed from Q and U. As has always been done, the uv data are first Fourier Transformed (FTed) into the map plane which results in an image (the ‘dirty image’) which is the convolution of the FT of the antenna distribution in the uv plane (the ‘dirty beam’) with the source sky brightness distribution. The dirty beam is then deconvolved from the dirty image (i.e. it is ‘cleaned’) to find an image of the source. The Clark method (Clark 1980) of separating the cleaning process into major and minor cycles, treating each Stokes plane separately, was used.

The broad bandwidths of the EVLA WIDAR correlator, however, introduce some new imaging requirements and considerations that were, for the most part, unnecessary with the VLA. These are described briefly here:

a) Bandwidth smearing: If the observations had not been in spectral line mode, then the broad frequency band would have introduced severe chromatic aberration into the image; this aberration worsens with distance from the map center. However, since spectral line mode is being universally employed at the EVLA, bandwidth smearing is instead restricted to the spectral resolution of the data (by using the multifrequency synthesis technique, see next section). For example, for our data at the center of either band and at a distance from the map center that is twice the FWHM of the primary beam, the loss in amplitude due to bandwidth smearing is only about 1.5%, or essentially negligible where most of the emission occurs.

b) Multi-frequency synthesis (mfs): The positions of the antennas in the uv plane are measured in wavelengths and those positions will vary as the frequency changes across a given band. Consequently, if each spectral channel is gridded separately, there is an improvement in uv coverage over a case in which channels are averaged together. The clean algorithm employed in CASA utilizes this multi-frequency synthesis technique (Conway, Cornwell, & Wilkinson 1990, also called ‘bandwidth synthesis’).

c) Widefield imaging: The sensitivity of the array to emission that is far from the map center and even outside of the telescope’s primary beam means that the array itself is non-coplanar to such emission. Thus, the ‘w term’ in the FT (the coordinate in the line-of-sight

direction towards the source), which can be ignored near the map center, becomes important. CASA clean employs the ‘w-projection algorithm’ (Cornwell, Golap, & Bhatnagar 2008) to correct for this effect.

d) Spectral index fitting: With wide bands, the spectral index of the source itself, which is spatially variable, needs to be fitted during imaging (Sault & Wieringa 1994). In CASA’s clean algorithm, this is accomplished by assuming that the emission at any position can be described by,

$$I_\nu = I_{\nu_0} \left(\frac{\nu}{\nu_0} \right)^{\alpha + \beta \log\left(\frac{\nu}{\nu_0}\right)} \quad (5)$$

where ν_0 is a reference frequency within the band (here taken to be the band center), I_{ν_0} is the specific intensity at the reference frequency, α is the spectral index and β describes the spectral curvature. The function is expanded in a Taylor series about ν_0 , resulting in a polynomial fit to the spectrum. The fit includes all unflagged channels across any given band and is not done on a ‘per spectral window’ basis. In addition, the fitting is done using all data so that the resulting parameters correspond to a single spatial resolution (for example, the α map is not formed such that the spatial resolution would vary across the band)¹³. Rau & Cornwell (2011) outline the implementation of spectral fitting and provide examples as to how the image can improve with increasing numbers of Taylor terms, n_T .

e) Multi-scale clean: Improvements have been made over the traditional clean which modeled all emission as a collection of point sources. The clean implementation in CASA now allows for a multi-scale clean (Cornwell 2008) which assumes that the emission can be modeled as a collection of components over a variety of spatial scales. These scales are typically chosen to span the range from an angular size of ‘zero’ (corresponding to a point source, or the classic clean analogy) to a scale of order the maximum spatial scale expected to be present in the emission. Since the latter is not always known in advance, in practice, the maximum scale size is increased systematically until no more flux is actually cleaned out in that largest scale¹⁴.

¹³At the time of writing, this is the only CASA-based fitting function that is available.

¹⁴If the flux becomes negative in the largest scale, the trial is

For details of the CASA implementation of the combined multi-scale, multi-frequency synthesis (ms-mfs) clean, see Rau & Cornwell (2011).

f) Primary beam: The primary beam (PB) varies from one end of the band to the other and, as a result, nowhere in the field of view is there a ‘null’ as there would be for a monochromatic primary beam (Bhatnagar et al. 2011). Consequently, it is the frequency-averaged PB (PB_{avg}) that the final cleaned image must be corrected for. Moreover, since the frequency dependence of the PB imposes its own spectral index across the field of view, all spectral index maps (Sect. 2.6) must be corrected for this effect as well.

NGC 4631 was mapped taking into account all of the above points.

At both bands, a very wide field was first mapped (3 degrees for L-band, or 6 times the primary beam FWHM; 34.1 arcmin for C-band or 4.6 times the primary beam) to determine how large an image needed to be mapped to include all sources of significant flux in the clean. Smaller fields were then mapped completely, as required. For the multi-scale clean, we used typically 4 to 6 equally-spaced spatial scales, the first one always corresponding to point sources as in the classic clean. For example, at L-band, scales up to 4.2 arcmin were employed, where the largest scale was chosen according to the considerations of point *e)* above. We also self-calibrated each data set once, finding that a single amplitude + phase self-calibration resulted in a small improvement in the rms map noise¹⁵.

After extensive experimentation, we adopted 3 sets of parameters representing 3 different spatial resolutions for each frequency and display them, along with some ancillary data, in Figs. 1 and 2; the corresponding map parameters are given in Table 2.

The theoretical noise values for these observations (including confusion estimates) are 18 and $3.7 \mu\text{Jy beam}^{-1}$ at L-band and C-band, respectively. Our lowest rms noise values are only 1.6 and 1.3 times higher for the total intensity images. There are, however, several residual linear cleaning artifacts in the L-band images that are

aborted and the maximum scale is decreased until positive flux is cleaned in all scales.

¹⁵A phase-only self-calibration did not improve the results.

visible immediately to the east and west of the galaxy’s disk (see Fig. 1c in particular). The conclusions that we present in this paper are not affected by these artifacts. The disconnected emission seen approximately 2 arcmin above and below the plane in Fig. 2c is likely real and part of the halo; missing low-order spacings contribute to the well-known appearance of the galaxy’s disk emission sitting on a negative bowl.

Note that, as is usually done, all displayed total intensity images are not corrected for the primary beam in order to show images with uniform noise. When numerical results are given, however, the results have been corrected for the frequency-averaged primary beam (PB_{avg}). Note also, that we carried out some subsequent analysis using AIPS.

2.5. Polarization Imaging

Stokes Q and U maps were formed with the same sets of parameters as the total intensity images, except that fewer spatial scales were required during cleaning, given the weaker emission in these maps. The relevant parameters for these images are given in Table 2. In principle, the rms noise on the Q and U maps should be the same as the I map; however, the lower signal in the cross-hands means that residual errors associated with cleaning the high intensity emission are no longer present. At L-band, our lowest rms noise is 1.2 times the theoretical value and at C-band, our lowest noise matches the theoretical value. Note that, in order to obtain sufficient signal-to-noise (S/N) in the polarized emission, all spectral windows were used.

We formed polarized intensity images, $P = \sqrt{Q^2 + U^2}$, for each of the uv weightings of Figs. 1 and 2, correcting for the bias introduced by the fact that P images do not obey Gaussian statistics (Simmons & Stewart 1985; Vaillancourt 2006). Maps of the polarization angle of the electric field vector, $\chi = (1/2)\arctan(U/Q)$, were also formed for points for which the linear polarization was $> 4\sigma$ ¹⁶. When displayed, we have rotated χ by 90 degrees to illustrate the observed (uncorrected for internal Faraday rotation) direction of the magnetic field. We show the results for only a single

¹⁶The cutoff for χ was relaxed slightly from 5σ in order to show the trends in vector orientation with position.

representative data set in the two frequency bands (Robust = 2 for L-band and Robust = 0 + uv taper for C-band) in Fig. 3¹⁷. Consistent with the total intensity images (Sect. 2.4) the displayed maps are shown without primary beam corrections.

We then carried out a PB correction using the same frequency-averaged primary beam, PB_{avg} , as was used for the total intensity images. This correction is good to zeroth order, but does not take into account first order effects which would result from differences between the right and left circularly polarized PBs. First order corrections are not yet implemented in CASA but we expect them to be small for this data set. For example, if the difference between the right and left circularly polarized PB voltage response is of order 10% at a distance from the map center corresponding to 30% of the primary beam (17.4 arcmin and 4.6 arcmin at L-band and C-band, respectively), then the error in Q or U would be 3% of the Q or U intensity at that point.

PB corrections of the linearly polarized intensity maps shown in Fig. 3 of all emission greater than 5σ resulted in increases in flux of 5% and 40% at L-band and C-band, respectively. Maps of χ (shown in Fig. 3) do not require PB correction.

We then formed maps of percentage polarization for the two bands (these also do not require PB correction). The maps were formed for emission which was greater than 5σ in both linear polarization intensity as well as total intensity, ensuring that the spatial resolutions are matched. We do not display the L-band maps since the result had sufficient S/N in only 20 beams and these positions were non-contiguous spatially. The C-band percentage polarization map is shown in Fig. 4. We calculated the average percentage polarization over the region shown by measuring the total polarized flux (rather than per pixel values) and dividing by the total flux, so that high values around the periphery of the emission do not skew the result; we find an average of 7.0% for the result corresponding to the region displayed. This region is mainly in the disk where some Faraday depolarization may be occurring (Sect. 3.2).

¹⁷Note that the CASA package did not allow for variable vector lengths, hence they are drawn as constants in these figures.

2.6. Formation of Spectral Index Maps

As indicated in Sect. 2.4 point *d*), the wide bands that are now available at the EVLA make it possible, in principle, to create spatially resolved spectral index maps, α , (and curvature maps, β , if there were sufficient signal-to-noise) over a single band with a single observation and common spatial resolution. One could form a map of α for L-band and for C-band individually, and then form such a map between the two bands, assuming a constant spectral index between the two bands.

For observations at two frequencies with a single EVLA array, as for our C-array test observations, however, there are some limitations. First, as specified in Paper I, we do not detect spatial scales at L-band and C-band that are greater than 16.2 and 4 arcmin, respectively¹⁸. The halo of NGC 4631 at both bands has previously been observed to extend to approximately 12 arcmin (see, for example, Fig. 9 of Hummel, Beck, & Dettmar (1991) and Fig. 3 of Golla & Hummel (1994)). It is therefore clear that not all flux has been detected at C-band and, as Fig. 1 illustrates, the broadest scale halo emission has not been detected at L-band either. Future D-array observations, with additional shorter spacings, should remedy this situation at L-band.

Using previously published total flux estimates, we can normally quantify the amount of flux that has been missed in our observations. However, at C-band, a wide range of 4.85 GHz fluxes have been reported, likely reflecting similar problems with spatial scales, for example, $S_{4.8GHz} = 438$ mJy, 243 mJy (see NED) and 480 mJy (Golla & Hummel 1994). Our primary-beam-corrected flux in C-band is $S_{6GHz} = 180$ mJy. Using the average global spectral index of Hummel & Dettmar (1990), $\alpha_{avg} = -0.73$, our frequency-adjusted flux would be $S_{4.8GHz} = 210$ mJy, indicating that there is significant flux missing from the C-band maps. We thus do not show our C-band spectral index maps in this paper.

¹⁸These values are for full-synthesis observations. For short observations of \lesssim one minute duration (snapshots) these values could reduce to as little as 8 and 2 arcmin, respectively (see *Observational Status Summary* at <http://evlaguides.nrao.edu>). Our observations (see Table 1) are intermediate between a snapshot and full synthesis. Consequently, the spatial scales quoted in the text are likely upper limits.

At L-band, we do form spectral index maps. The primary-beam-corrected flux from these C-array observations is $S_{1.5GHz} = 935$ mJy, or 77% of the VLA D-array VLA fluxes of 1.22 Jy at $\nu = 1.49$ GHz (Hummel & Dettmar 1990) or 1.29 Jy from the Westerbork Synthesis Radio Telescope at $\nu = 1.365$ GHz (Braun et al. 2007)¹⁹. Since the missing flux is on the largest scales, we form spectral index maps at L-band beginning with the highest resolution image (Fig. 1)a, and then consider how this and other errors affect the result. Since the L-band 500 MHz bandwidth is much narrower than the frequency spacing which has been used in the past to calculate α (e.g. 610 MHz to 1412 MHz, or 4.75 GHz to 10.7 GHz, see Werner 1988), the values of α presented here can be thought of as tangents to the frequency spectrum at each spatial position in L-band.

Spectral index and curvature maps were formed from ratios of the Taylor expansion coefficient maps which describe Eqn. 5²⁰, after first correcting these coefficient maps for PB_{avg} and then introducing a 5σ total intensity cut-off. It has been shown that increasing the number of terms to the polynomial fit will generally improve the result, subject to S/N considerations (Rau & Cornwell 2011). For example, fitting both α and β allows α to be well-determined at the reference frequency even though β may not have sufficient S/N in each synthesized beam to be presented as a map. In Fig. 5 we show spectral index maps corresponding to the high resolution L-band data (Fig. 1a) for a straight spectral index assumption (a) and then allowing for curvature within the band (b).

The ‘‘mottled’’ appearance of the two maps is due in part to the fact that point-to-point variations are significant. For example, after subtracting the two spectral index maps, the rms of the result is $\sigma \approx 0.4$ (omitting approximately a beam width around the perimeter of the emission) suggesting that the per-pixel error from the fitting is of this order. There are, however, variations in the map that exceed this uncertainty. In addition, there are some global trends in α which are very similar between the two maps and the aver-

age spectral indices ($\bar{\alpha}$, averaged over the maps) are in very good agreement, differing by only 0.01. Clearly, the error bar on the spectral index decreases with the number of points that are averaged, i.e. with increasing S/N, as one would expect; we will return to this point in Sect. 3.3.

Regarding the effect of missing broad scale flux, our measured α will not be affected provided the broad scale emission has the same spectral index as the disk and contributes a constant intensity at each position. It is known, however, that the halo spectral index, which we associate with the broad scale emission, is steeper than that of the disk. A variety of measurements have been made over different frequency ranges, but typically, off-major-axis values fall in the range, $\alpha = -0.9 \rightarrow -2$ (see discussion in Hummel & Dettmar 1990).

Taking the extreme case of $\alpha = -2$, we can determine how the addition of a ‘plateau’ of emission of this spectral index to our data would affect our measured values of α . If the halo emission occupies an emission ellipse of major \times minor axis extent, approximately 15 arcmin \times 12 arcmin (Hummel et al. 1988), then the emission region of Fig. 5 occupies approximately 20% of this area. Scaling the missing flux of Fig. 1a to this area, assuming that the broad scale flux uniformly fills the emission ellipse, then the missing emission corresponds to a plateau of 0.12 mJy beam⁻¹, on average, over the disk at the central frequency.

Using the measured average intensity from Fig. 1a over the same region as the spectral index (taking $\beta = 0$) the addition of such a steep spectral index plateau would adjust our measurement of α from -0.84 to -0.88 ($\Delta\alpha = 0.04$). This is a worst-case scenario unless there are missing spatial scales that are *smaller* than 11 arcmin (the major axis size).

Spectral index, α , and curvature, β , maps for L-band were also formed for the remaining mid and low resolution maps corresponding to Fig. 1b and c, respectively and are shown in Fig. 6. For these resolutions, we find $\bar{\alpha} = -0.82$ and $\bar{\alpha} = -0.87$, respectively. The curvature, $\bar{\beta}$, averaged over the emission regions for these two resolutions is 1.9 in both cases, agreeing to within ± 0.1 with the result at high resolution. If we consider fitting errors, possible errors from missing flux, and variations between the different uv weightings, our average spectral index is $\bar{\alpha} = -0.84 \pm 0.05$.

¹⁹The NRAO VLA Sky Survey (NVSS) flux of 981.6 mJy has been underestimated for this galaxy (see Condon et al. 2002).

²⁰ $\alpha = TT1/TT0$ and $\beta = TT2/TT0 - \alpha(\alpha - 1)/2$, where $TT0$, $TT1$, and $TT2$ are maps of the first 3 Taylor terms.

As mentioned earlier, it is worth stressing that the wide bands used here allow for considerable flexibility in ‘tuning’ the spatial resolution of the array by appropriate use of uv weighting. This means that the spatial resolutions of L-band and C-band data can actually be matched exactly, even with observations in only a single array configuration. Therefore spectral index maps can also be made between L and C-bands from observations in a single array configuration. Although we formed such maps for NGC 4631, we defer the results until all missing C-band flux is recovered through additional observations (Paper I).

3. Results and Discussion

These new EVLA observations, even though they were obtained during a limited test run in a single array configuration (Table 1), have revealed a number of new features not before seen in NGC 4631. In this section, our intention is not to make an exhaustive list of all features, but rather summarize the more obvious or new results and to place them in the context of previous knowledge of this galaxy.

3.1. Total Intensity Images and Comparison with other Wavebands

The total intensity images displayed in Figs. 1 and 2 show numerous extensions away from the plane at both frequencies.

At L-band, in particular, two of the more prominent features appear in projection as loops or partial loops (although they could represent shells) that have been outlined in red in Fig. 1b. Although we have noted a few cleaning artifacts in this image to the east and west of the major axis of the galaxy (Sect. 2.4), the loops do not fall within the affected regions and they are either of sufficient signal-to-noise and/or persistent over various uv weightings (some not displayed here but formed during experimentation with uv weightings as described in Sect. 2.4) that we consider them to be real features.

The diameter of the larger northern loop, which is only partial in Fig. 1b, is 6.3 kpc. It is also visible in the lower resolution Fig. 1c where it appears to ‘frame’ the companion dwarf elliptical galaxy, NGC4627 which is 2.6 arcmin to the NW of the galaxy’s center. This is likely a coincidence, since

we will show below that the loop is related to the hot X-ray gas.

The diameter of the smaller more easterly loop is 2.6 kpc and this loop becomes ‘filled in’ in the lower resolution Fig. 1c. The eastern side of this loop and the weaker emission that extends upwards from it corresponds to the HI ‘worm’ observed by Rand & van der Hulst (1993). The latter feature sits above a significant HI supershell found by those authors whose diameter (3 kpc) is approximately the same as our eastern loop. It is likely that these features are related and are associated with star forming regions that are present in the underlying disk. The closest prominent star formation complex is located at RA $\approx 12^{\text{h}} 42^{\text{m}} 22^{\text{s}}$, DEC $\approx 32^{\circ} 32' 42''$; it is marked with a cross in the H α map of Fig. 2c.

A search of previous radio continuum images of NGC 4631 (Hummel et al. 1988; Hummel & Dettmar 1990; Hummel, Beck, & Dettmar 1991; Golla & Hummel 1994; Dumke et al. 1995; Golla 1999; Braun et al. 2007; Krause 2009; Heald et al. 2009) does not reveal these loops, although the continuum image in Braun et al. (2007) shows hints of the larger central loop. Since we see extraplanar structure on all scales in this galaxy, detecting specific features requires appropriately weighted uv data over scales that match the feature of interest. The spatial scales highlighted by our new data have now revealed these loops and the other arcs and filaments that we see extending from the plane. It is possible that some of the other broad extensions (for example, at RA $\approx 12^{\text{h}} 42^{\text{m}} 12^{\text{s}}$, DEC $\approx 32^{\circ} 31' 30''$) would resolve into loops if viewed at higher resolution and sensitivity.

The close connection between X-ray emission and the radio halo, first pointed out for this galaxy by Wang et al. (1995) and Wang et al. (2001), finds stronger support in these observations. In Fig. 7, we show the soft X-ray emission from Fig. 1a, enhanced to show extra-planar emission, together with the low resolution L-band image from Fig. 1c. In this figure, we see that the X-ray emission forms a loop interior to the northern radio continuum loop, suggesting that hot gas may be confined by magnetic pressure. It is interesting that there is even a smaller vertical X-ray protrusion (RA $\approx 12^{\text{h}} 42^{\text{m}} 07^{\text{s}}$, DEC $\approx 32^{\circ} 36'$) above the gap on the north-eastern side of the radio continuum loop. A close relationship has been found be-

tween radio continuum and X-ray emission in the outflow of NGC 253 as well (Heesen et al. 2011).

We can determine whether such confinement is feasible, assuming a simple case of unity filling factors, by estimating the minimum energy magnetic field strength following Beck & Krause (2005). Assuming a proton to electron number density ratio of 100, a line of sight distance equal to the width of the radio loop as shown in Fig. 7, an isotropic field direction, and a spectral index equal to the global average disk value, we find $B_{min} \approx 8 \mu\text{G}$. The magnetic pressure is then $P_{mag} = 3 \times 10^{-12} \text{ erg cm}^{-3}$. By comparison, the thermal pressure from the hot, X-ray-emitting gas is $P_{th} = 6.9 \times 10^{-13}$ (Wang et al. 2001), implying that magnetic pressure is indeed sufficient to confine the thermal gas.

At C-band, where we have higher spatial resolution (Fig. 2), we continue to see many vertical extensions. Again, we do not discuss every feature, but point out the brightest extension which is on the north of the disk at RA = $12^{\text{h}} 42^{\text{m}} 09^{\text{s}}$, DEC = $32^{\circ} 33' 10''$, and best seen in Fig. 2b. This extension is directly below the west side of the large northern loop seen in Fig. 1b. This feature protrudes 1 kpc above the main emission below it, or about 1.6 kpc from mid-plane. The detail and numerous extensions observed on this map reveal the complexity of the disk-halo interface in this galaxy.

The disconnected ‘patches’ of emission visible in Fig. 2c above and below the plane appear to represent brighter parts of the broader scale halo emission which has not been detected in its entirety in our data due to missing short spacings at C-band (Sect. 2.4). The feature at RA $\approx 12^{\text{h}} 42^{\text{m}} 23^{\text{s}}$, DEC $\approx 32^{\circ} 34' 30''$ for example, corresponds to the HI worm mentioned above.

The well-known close relationship between radio continuum, H α , and CO emission is also evident from Fig. 2, to the extent that ‘kinks’, widenings and narrowings along the major axis are correlated between these components. Radio continuum and H α peaks are nicely coincident in the wider ‘bulge’ region (Irwin et al. 2011) about 3 arcmin to the east of the galaxy’s center within which the bright star formation complex mentioned above is located.

3.2. Polarization Maps

The linear polarization maps with observed magnetic field vectors are shown in Fig. 3 and the percentage polarization with observed magnetic field vectors for C-band is shown in Fig. 4. Recall that the Q and U images have lower rms than the total intensity images (Sect. 2.5) and hence some polarized emission can be seen outside of regions of total intensity.

All maps have been corrected for foreground ionospheric Faraday rotation, where necessary (Sect. 2.3), but no Faraday rotation correction has been done for the galaxy itself²¹; therefore, especially in the disk at L-band, we expect significant Faraday depolarization, as indicated in Sect. 2.5. This is evident in Fig. 3a which shows little polarized intensity in the disk at L-band. Previous L-band images (see especially Heald et al. 2009; Hummel, Beck, & Dettmar 1991) similarly show little or no polarization right in the disk. The halo, however, should not be as strongly affected. The effects of Faraday rotation should also be lower at C-band (Fig. 3b) but will not be negligible in the disk. For example, rotation measures of up to $\pm 300 \text{ rad/m}^2$ have been found for NGC 4631 in a larger 85 arcsec beam (Krause 2004), corresponding to 43 degrees of rotation at 6 GHz; the value could be higher still in our data set, given our smaller beam. Again, away from the plane, Faraday rotation should be minor, as has been demonstrated previously for the halo region of the edge-on galaxy, NGC 5775 (Soida et al. 2011, cf. Figs. 3 and 5 of that paper). Nevertheless, we prefer to be cautious about our comments regarding the magnetic field orientation in the following discussion.

At L-band, the most prominent halo feature is a highly linearly polarized spur located at RA $\approx 12^{\text{h}} 42^{\text{m}} 20^{\text{s}}$, DEC $\approx 32^{\circ} 34' 30''$. This spur is visible in the linearly polarized map of Heald et al. (2009) and also in the lower resolution 5 GHz map of Golla & Hummel (1994). The spur is directly above the eastern radio continuum loop and may be related to the disturbance that has caused that loop as well as the HI supershell below it (Sect. 3.1). However, the galaxy also displays an V-shaped field structure on the northern side (or ‘X-shaped’ globally, see above references) and this

²¹We will carry out such an analysis in a future paper.

spur may be associated with the eastern side of that larger feature.

At 6 GHz (Fig. 3b, Fig. 4), it is interesting that the observed magnetic field orientation within the disk is parallel to the disk. Previously published maps have shown the magnetic fields near the center of NGC 4631 to be perpendicular to the disk (for example, see the 8 GHz image of Krause 2004, at 84 arcsec resolution), although at larger radii the fields are parallel to the disk again (Krause 2009). Our 12 arcsec observations and omission of the largest spatial scales are targeting different scales and may now be revealing a disk-parallel component near the galaxy’s center, although Faraday-corrected maps are still required to confirm this. Away from the disk, the magnetic field tends to become perpendicular to the plane, in agreement with previous observations. Extra-planar polarized emission both to the north-east and north-west of the galaxy’s center agrees in general with the image of Golla & Hummel (1994) at 5 GHz.

A final point of interest is the sharpness with which the *apparent* magnetic field orientation changes (90 degrees within a single beam) at RA $\approx 12^{\text{h}} 42^{\text{m}} 12^{\text{s}}$, DEC $\approx 32^{\circ} 32' 30''$ (see Fig. 4). This change occurs at the location of a bright HII region complex visible in Fig. 2c which has been labelled CM67 by Golla (1999). If such a change is still visible after having corrected for Faraday rotation, then it lends support for the notion that the magnetic field is swept outwards with the outflow from specific star forming regions. Note that there are radio continuum spurs above and below this location (Fig. 2c). If the change is not intrinsic but is due to Faraday rotation alone, then either the ordered magnetic field in the line of sight has changed sharply at this position or the electron density has changed abruptly, or both. In either case, CM67 is an important region for follow-up studies with applied rotation measure corrections.

3.3. Spectral Index Images

Our L-band spectral index maps (Figs. 5 and 6) are the first that have been formed from *within* an observing band for an edge-on galaxy and represent a tangent to the spectrum at 1.5 GHz, rather than an average between broadly separated frequencies as has been done in the past.

The average spectral index is $\bar{\alpha} = -0.84 \pm 0.05$ (Sect. 2.6) and therefore the L-band maps are clearly dominated by non-thermal emission. This result is typical of the values found in other galaxies (Niklas, Klein, & Wielebinski 1997) and the Milky Way (Reich, Reich & Testori 2004; Strong, Orlando, & Jaffe 2011). Previous values for the disk of NGC 4631 cover a rather wide range (see Hummel & Dettmar 1990), for example, -0.68 (from 610 MHz and 10.7 GHz measurements), -0.45 (from 327 MHz and 1.49 GHz), -0.69 (from 327 MHz, 610 MHz, 1412 MHz, and 10.7 GHz data), and -0.9 (from 610 MHz and 1412 MHz).

Also, although the global spectral index of NGC 4631 has been studied extensively (Klein et al. 1984; Sukumar & Velusamy 1985; Werner 1988; Hummel & Dettmar 1990; Pohl & Schlickeiser 1990) the only previous spectral index *maps* that have been published can be found in Werner (1988) whose highest resolution was 58 arcsec. Our maps are the highest resolution spectral index maps yet presented for this galaxy.

The average, global spectral curvature is positive ($\beta = 1.9$, Sect. 2.6). The most likely explanation is the contribution of thermal emission from the disk. To see whether this is feasible, we use the thermal flux density estimate of Golla (1999) of $F_T(4.86 \text{ GHz}) = 56 \text{ mJy}$ who makes use of the H α luminosity of NGC 4631 and adjusts upwards to account (roughly) for dust obscuration. Extrapolated to 1.5 GHz with a $\nu^{-0.1}$ frequency dependence gives $F_T(1.5 \text{ GHz}) = 63 \text{ mJy}$ with a variation of 2 mJy across L-band. The curvature that we have found from Eqn. 5 corresponds to an increase of 2% at the upper frequency band edge in comparison to a non-curving spectral index. With a total flux density of 935 mJy at the band center (Sect. 2.6), a curved spectral index results in an increase of 16 mJy at the high frequency end of the observing band, over the value that would be observed if the spectral index were constant. This increase is less than the estimated thermal flux density at the upper end of the band, so it is clear that a thermal contribution is capable of accounting for the observed curvature. However, thermal emission contributes, on average, less than 7% of the flux at L-band, assuming that the thermal estimate of Golla (1999) can be applied.

An interesting result is the detail with which we

have mapped the spectral index distribution in a single observation in a single frequency band. As indicated in Sect. 2.6, the uncertainty at any point is approximately ± 0.4 , though it becomes lower depending on the size of the region over which averages are taken. For the average spectral index over all maps, the uncertainty is smaller, i.e. ± 0.05 . Consequently, in the following, we point out only values of α that are significant in comparison to the uncertainties which have been appropriately averaged over the region of interest and for which there are similar trends for all maps shown in Figs. 5 and 6.

For example, contrast in the spectral index is observed in the region of the eastern loop (see dashed arc in Fig. 1b). The contrast is most clearly seen in Figs. 6a and b. The average spectral index along the sides of the loop itself (all maps) is $\bar{\alpha} = -1.3$ and this value does not differ significantly from the underlying disk at the loop ‘footprints’. In the regions interior to the loop and just exterior to it, on the other hand, the values are much steeper (darker regions in Fig. 6a and b). The average spectral index interior to the loop is $\bar{\alpha} = -2.1$. Both values indicate that a thermal contribution will be negligible at these locations and, as we did in Sect. 3.1, we estimate a minimum energy magnetic field strength using the same assumptions as in that section but with these measured spectral indices. The result is $B_{min} \approx 17 \mu\text{G}$ along the loop²².

This is not the first time that spectral index contrasts or steep spectral indices have been observed in galaxies that experience outflows. For example, Lee et al. (2001) show that the spectral index of radio continuum features that are located along HI shells in NGC 5775 is flatter than in the interior and that this flattening cannot be due to a thermal contribution. As in NGC 4631, the spectral index along the loop itself is not significantly different from that of the underlying disk at its location. Moreover, although such steep spectral indices are not generally seen in our own Galaxy (Reich, Reich & Testori 2004; Strong, Orlando, & Jaffe 2011; Ghosh et al. 2011), Heesen et al. (2011) also find regions of very

steep spectral index in the galaxy, NGC 253, i.e. $\alpha = -2.0 \pm 0.2$ is seen within the outflow cone originating from the nuclear region of that galaxy. NGC 4631 is known to be experiencing widely distributed disk-related activity rather than a localized nuclear starburst (e.g. see Irwin et al. 2011), but the physics may be similar. For NGC 253, strong electron energy losses are implied, for example.

We defer the point-by-point decomposition of the map into thermal and non-thermal components to a future paper; nevertheless, it is possible to see evidence for the dominance of thermal emission in at least two specific star forming regions, best seen at the highest resolution spectral index maps (Fig. 5). One has been pointed out earlier (Sect. 3.1) and is marked with a cross on the H α map of Fig. 2c as well as the high resolution spectral index map of Fig. 5b. The spectral index at this position is $\alpha = -0.16 \pm 0.09$ (averaged from Fig. 5b over the star forming region) which is entirely consistent with a thermal spectrum, within uncertainties. Another star forming region located 1 arcmin to the SSW of this location and visible as a discrete peak in Fig. 2c also shows a similarly flat index, consistent with thermal emission.

4. Conclusions

In this paper, we have presented the first results from a new survey, called CHANG-ES, to observe radio continuum halos in 35 edge-on, normal spiral galaxies. The galaxies are being observed in all polarization products in two different bands, 1.5 GHz (L-band) and 6 GHz (C-band), and over 3 different EVLA array configurations. This is the first comprehensive radio continuum survey of halos to include all polarization products. The motivation and science goals for the survey have been presented in Paper I.

Our initial CHANG-ES test observations of NGC 4631 have been carried out at C array alone and therefore are sensitive to the disk, the disk-halo interface, and inner halo emission; we do not detect the faint large scale halo emission because of the lack of large scale sensitivity in this array configuration. Our new results demonstrate that, even with modest integration times, new details of the emission in this galaxy have emerged.

One advantage of the wide-band, multi-channel

²²By comparison, a classical calculation (Pacholczyk 1970) using a heavy particle to electron ratio of 40, and frequency limits from 10^7 to 10^{11} Hz, results in $B_{min} \approx 10 \mu\text{G}$.

EVLA capabilities is the ability to form spectral index maps at a common spatial resolution *within* a single observing band in a single array configuration. We have formed such maps at L-band. Our L-band spectral index map has the highest resolution yet obtained for this galaxy and is the first in-band spectral index map published for an edge-on galaxy. In addition, with appropriate uv weighting, the EVLA wide bands have allowed us to match spatial resolution between L-band and C-band in a single array configuration.

Our results for NGC 4631 include:

- At both 1.5 and 6 GHz, numerous extensions can be seen emerging from the disk into the halo, many of which have not previously been observed.

- At 1.5 GHz, two extra-planar features appear to form loops in projection. The larger loop is 6.3 kpc in diameter and located on the north side of the disk slightly to the west of center. The smaller loop, 2.6 kpc in diameter, is also on the north side of the disk but towards the east (see Fig. 1b).

- The larger loop is exterior to the soft X-ray feature observed by Wang et al. (2001) (Fig. 7). The minimum energy magnetic field is $8 \mu\text{G}$ and the magnetic pressure in this loop ($P_{mag} = 3 \times 10^{-12} \text{ erg cm}^{-3}$) is sufficient to constrain the hot X-ray gas ($P_{th} = 6.9 \times 10^{-13} \text{ erg cm}^{-3}$).

- The smaller loop is approximately at the location of the HI worm and supershell identified by Rand & van der Hulst (1993). The spectral index within and adjacent to the loop is much steeper ($\alpha \approx -2.1$) than along the loop itself ($\alpha \approx -1.3$).

- At 1.5 GHz, a spur of polarized emission can be seen away from the plane, consistent with previous observations; this spur is likely associated with the eastern loop.

- At 6 GHz, the polarization is higher and the average percentage polarization is 7% over regions within which the S/N was high enough to be measured, i.e. predominantly in the disk. The *apparent* magnetic field orientation in the plane of the disk (uncorrected for Faraday rotation) appears to be parallel to the disk.

- There is one position in the disk, corresponding to the HII region complex, CM67, at which the apparent field orientation changes sharply (Fig. 4); this is a target region for future in-depth analysis including Faraday rotation.

- At 1.5 GHz, the average spectral index is $\bar{\alpha} = -0.84 \pm 0.05$, indicating that the emission is predominantly non-thermal, on average, throughout the disk. However, a small thermal contribution is sufficient to explain the observed positive spectral curvature in this band.

- At specific discrete locations in the disk, it is clear that the thermal contribution is not negligible. An example is the location of a specific star forming region identified with a cross in Fig. 2c whose flat 1.5 GHz spectral index is consistent with thermal emission.

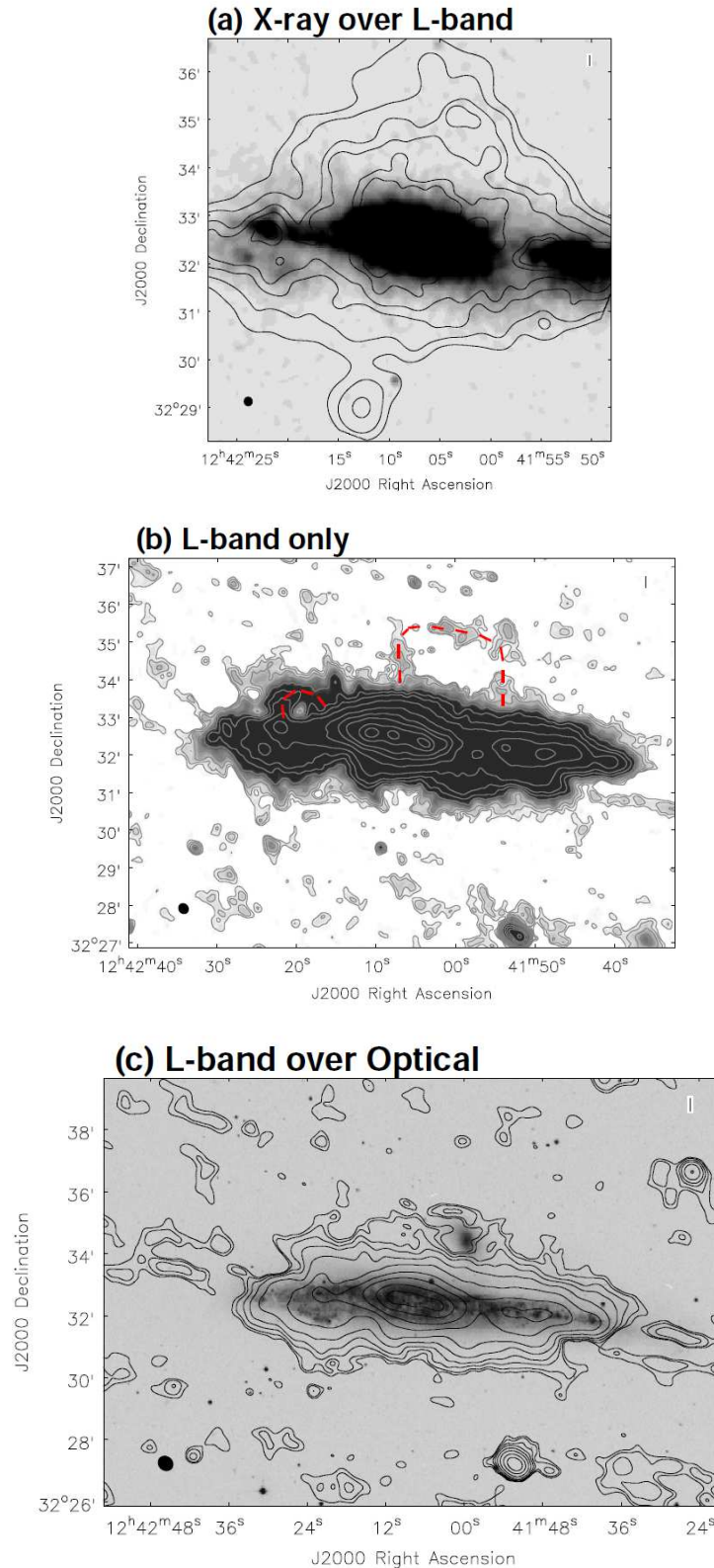


Fig. 1.— L-band (1.5 GHz) images of NGC 4631. The beam is shown as the filled ellipse at lower left. See Table 2 for map parameters **(a)**: Contours of soft X-ray emission (Wang et al. 2001) over the Robust 0 weighted greyscale image. **(b)**: Contours of the Robust 2 weighted image over a self-greyscale. Contours are at $9 (2\sigma)$, 13.5, 20, 30, 45, 65, 90, 150, 300, 500, 750, 1500, and $2500 \times 10 \mu\text{Jy beam}^{-1}$. Red dashed curves denote the loops discussed in Sect. 3. **(c)**: Contours of the uv tapered image over the Second Digitized Sky Survey (DSS2) blue image. Contours are at $2 (2\sigma)$, 3, 5, 8, 15, 30, 65, 120, 250, and $500 \times 100 \mu\text{Jy beam}^{-1}$.

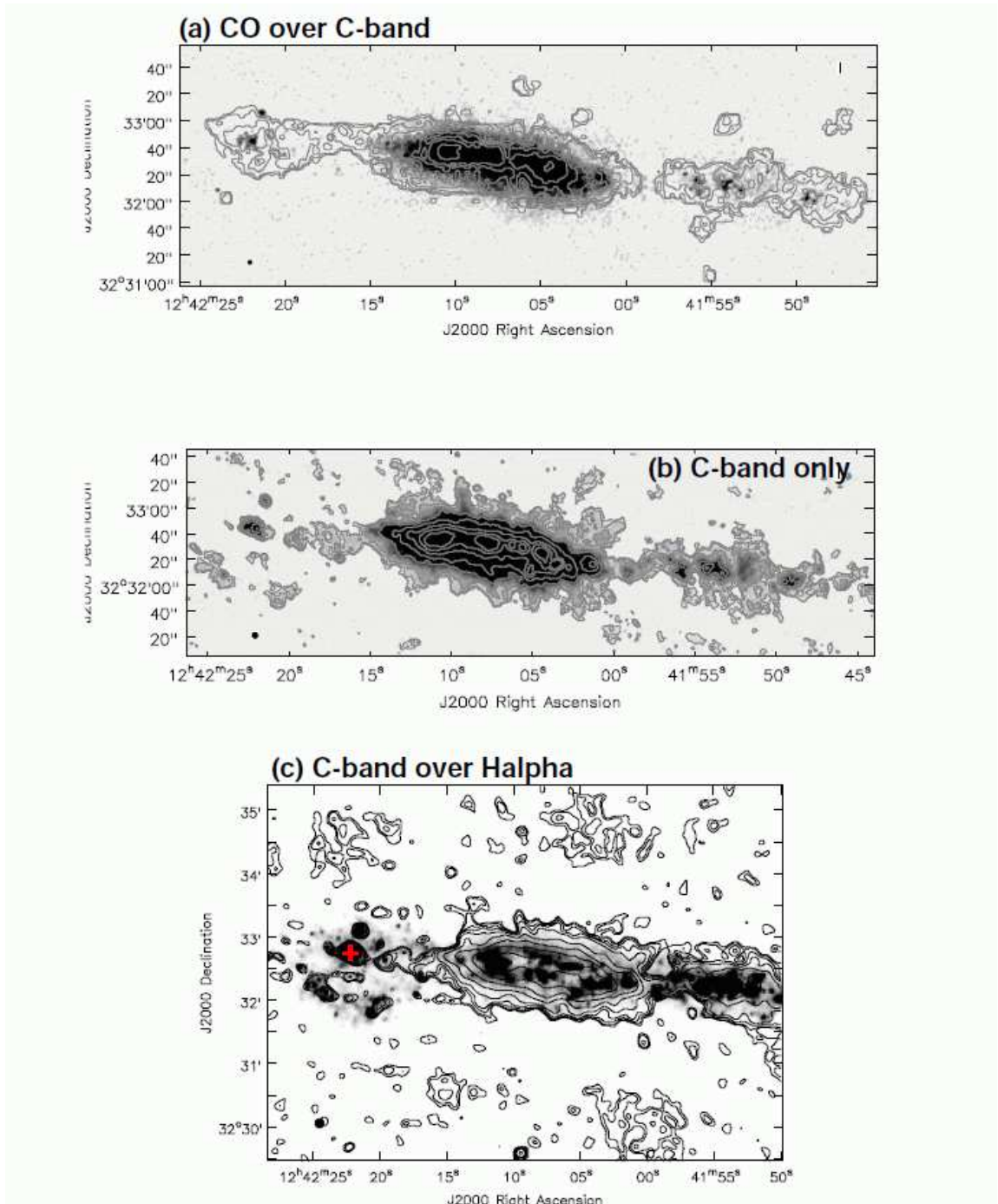


Fig. 2.— C-band (6 GHz) images of NGC 4631. The beam is shown as the filled ellipse at lower left. See Table 2 for map parameters. **(a)**: Contours of CO(J=3-2) emission (Irwin et al. 2011) over the Robust 0 weighted image. **(b)**: Contours of the Robust 2 weighted image over a self-greyscale. Contours are at 11 (2σ), 16.5, 30, 50, 80, 150, 300, 500, and 900 $\mu\text{Jy beam}^{-1}$. **(c)**: Contours of the uv tapered image over a greyscale of H α emission from Hoopes, Walterbos & Rand (1999). Contours are at 16 (2σ), 24, 40, 60, 100, 200, 400, 800 and 2500 $\mu\text{Jy beam}^{-1}$. The cross marks the location of a star formation complex discussed in Sect. 3.3.

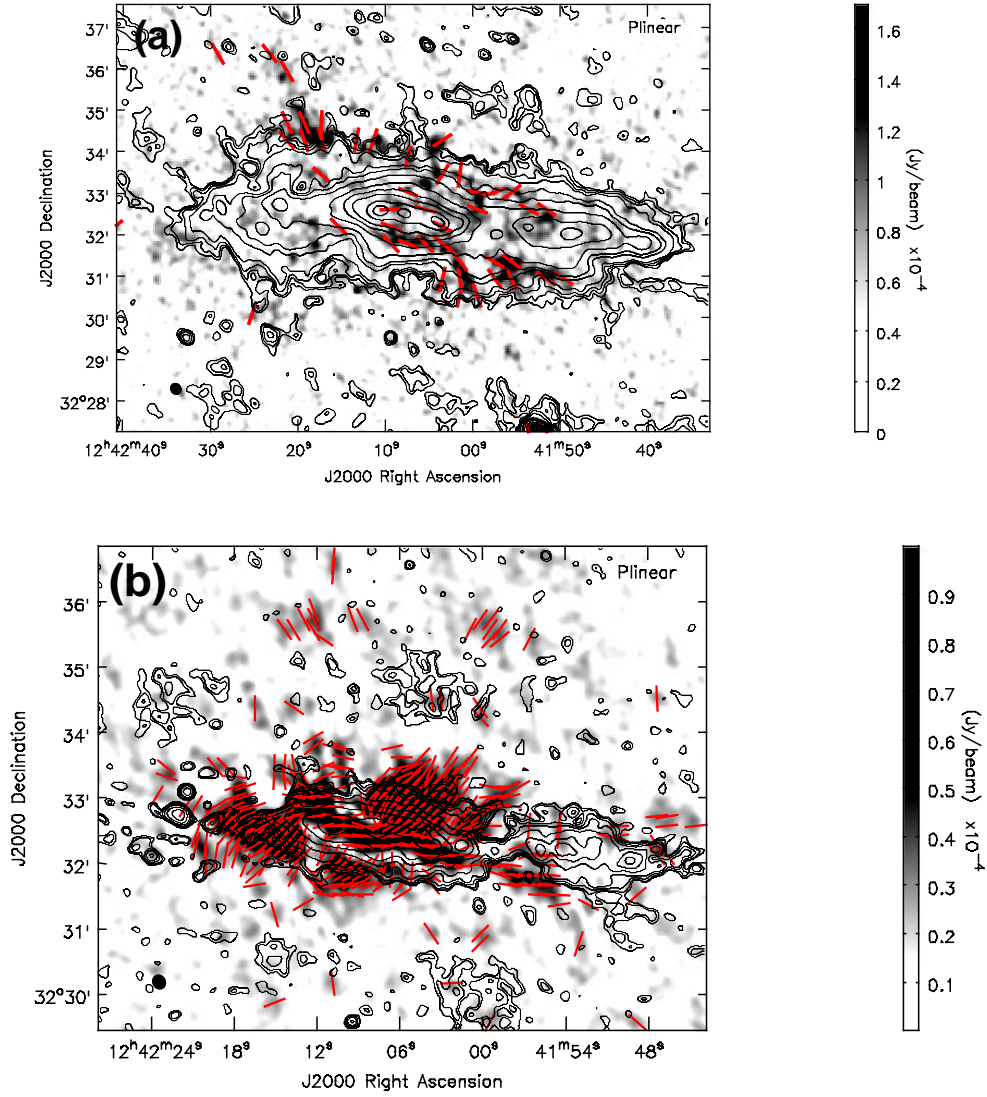


Fig. 3.— Polarization maps of NGC 4631. The linear polarization is shown in greyscale with the greyscale range shown at right. Contours show the total intensity emission, and red vectors show the apparent angle of the magnetic field. (Note that the vector length could only be specified as a constant in the CASA package.) Maps have been corrected for ionospheric Faraday rotation, but not for Faraday rotation intrinsic to the galaxy itself. The beam is shown as a filled ellipse at lower left. (a) L-band polarization corresponding to Fig. 1b. (b) C-band polarization corresponding to Fig. 2c.

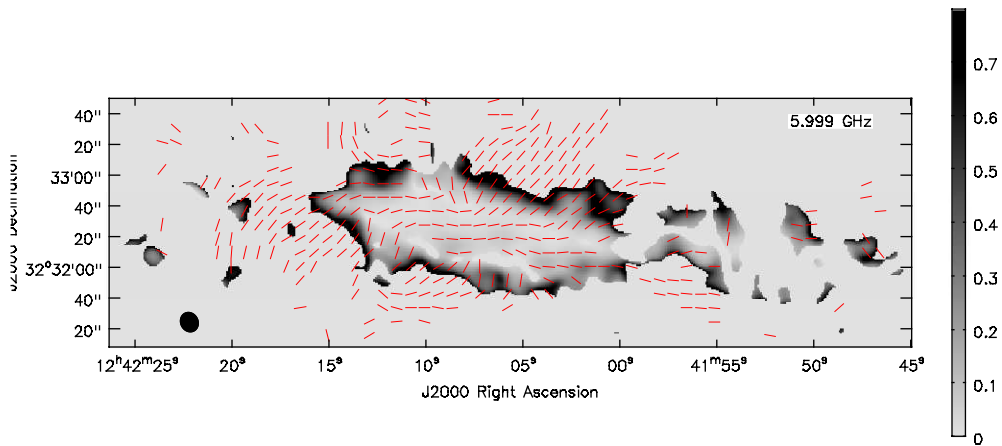


Fig. 4.— Map of percentage polarization at C-band superimposed with the apparent magnetic field vectors as shown in Fig. 3b. The greyscale range is shown at right and the beam ellipse is shown at bottom left. Notice the sharp change of vector orientation at RA \approx 12^h 42^m 12^s, DEC \approx 32[°] 32' 30^{''}.

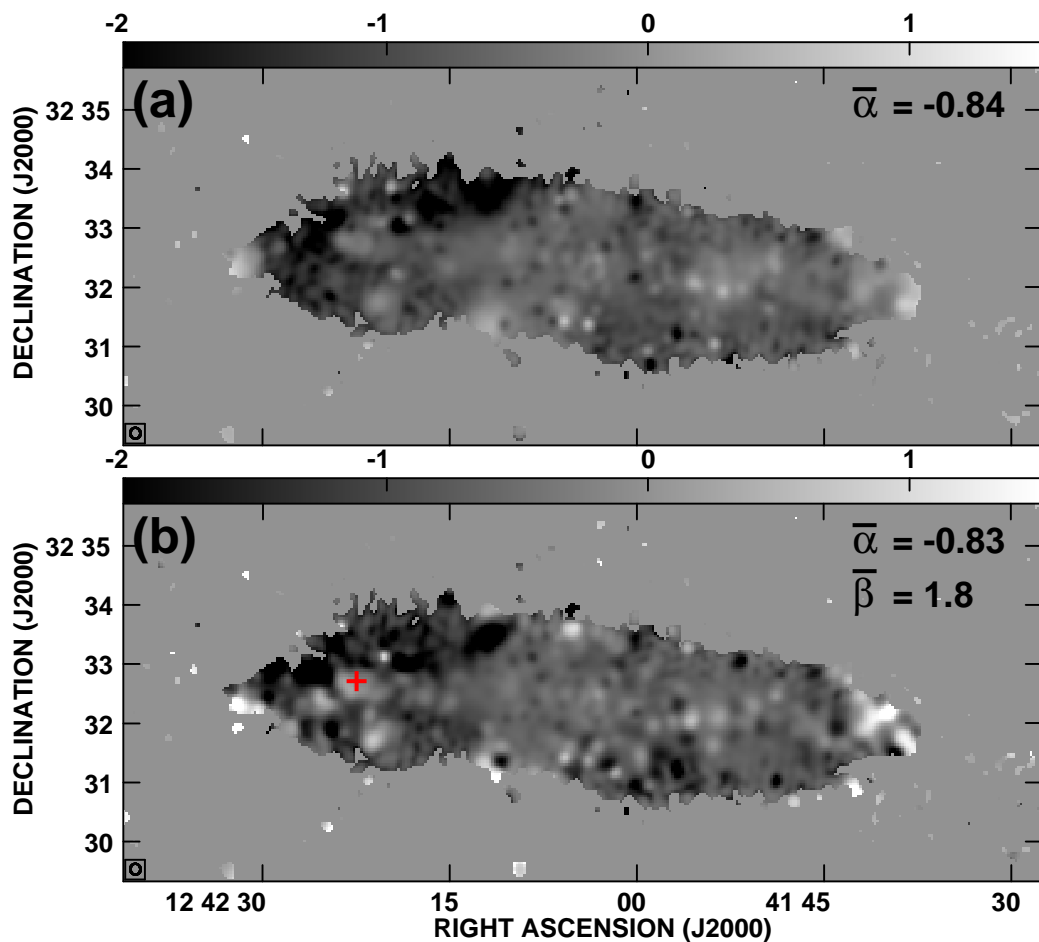


Fig. 5.— L-band spectral index maps corresponding to Fig. 1a, shown to the same greyscale and spatial scale. The spectral index and curvature (when fitted), averaged over the displayed emission, are denoted at upper right. The beam is indicated as an open ellipse at lower left. The per-pixel error bar is 0.4 (Sect. 2.6), creating the ‘mottled’ appearance; extreme values within a beam width of the perimeter are artifacts. **(a)** Fit to Eqn. 5 assuming no curvature ($\beta = 0$). **(b)** Fit to Eqn. 5, solving for both α and β . The cross marks the location of a star forming complex also marked in Fig. 2c.

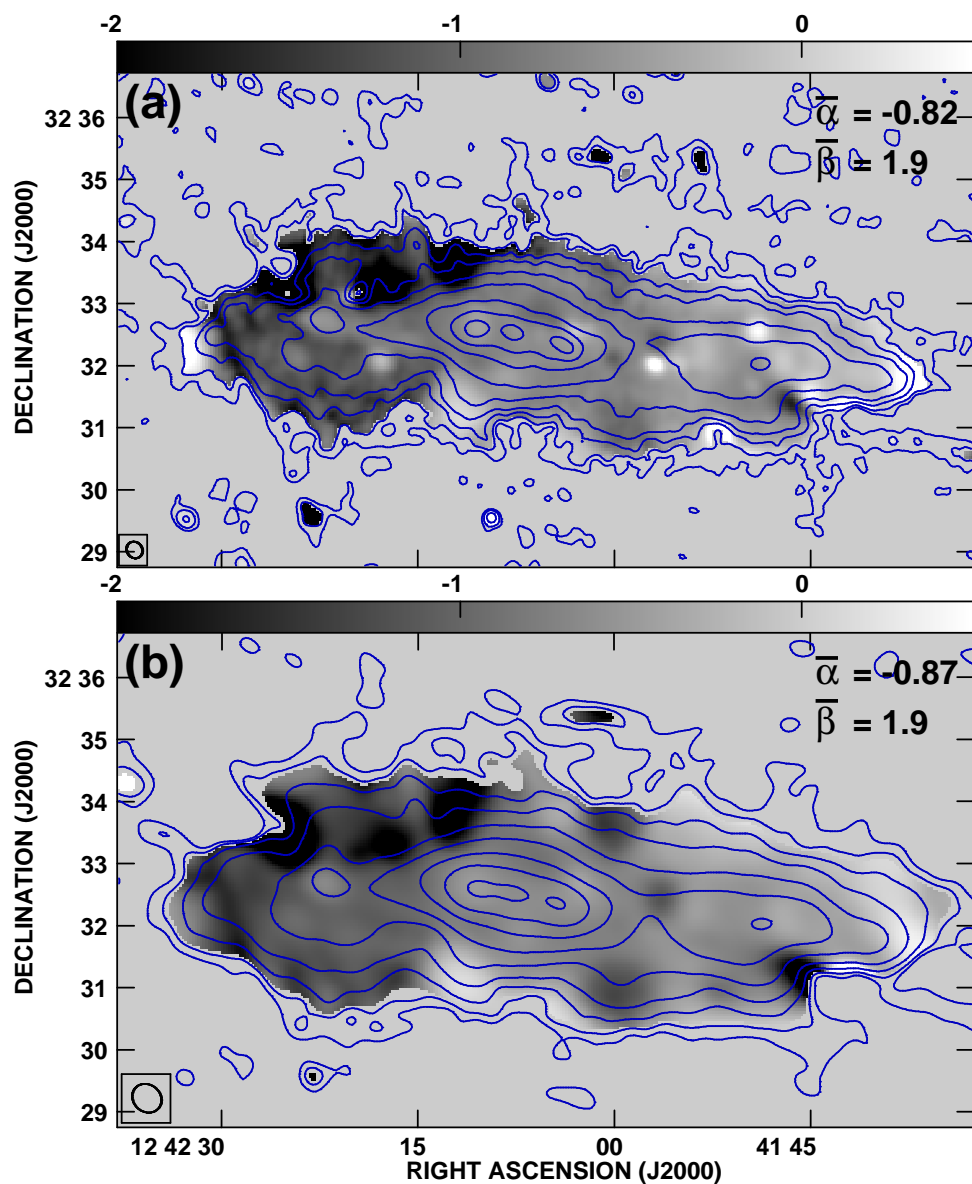


Fig. 6.— L-band spectral index maps of Fig. 1b and c, shown to the same greyscale (shown at top) and spatial scale. The spectral index and curvature, averaged over the displayed emission, are denoted at upper right. Contours are of the corresponding total emission. The beam is indicated as an open ellipse at lower left. **(a)** Maps corresponding to Fig. 1b. Contours are at 9 (2σ), 20 , 40 , 65 , 125 , 250 , 600 , 1200 , and $2400 \times 10^{-5} \text{ Jy beam}^{-1}$. **(b)** Maps corresponding to Fig. 1c. Contours are at 2 (2σ), 4 , 8 , 16 , 35 , 70 , 150 , 300 and $600 \times 10^{-4} \text{ Jy beam}^{-1}$.

JAI and DJS would like to thank the staff at the EVLA for their warm welcome and assistance during their sojourn in Socorro. Research at Ruhr-Universität, Bochum, is supported by Deutsche Forschungsgemeinschaft through grants, FOR1048 and FOR1254. The Digitized Sky Surveys were produced at the Space Telescope Science Institute under U.S. Government grant NAG W-2166. The Second Palomar Observatory Sky Survey (POSS-II) was made by the California Institute of Technology with funds from the National Science Foundation, the National Geographic Society, the Sloan Foundation, the Samuel Oschin Foundation, and the Eastman Kodak Corporation. The National Radio Astronomy Observatory is a facility of the National Science Foundation operated under cooperative agreement by Associated Universities, Inc.

Facilities: EVLA

REFERENCES

- Beck, R., & Krause, M. 2005, *Astron. Nachr.*, No. 6, 326, 414
- Bhatnagar, S., Rau, U., Green, D. A., & Rupen, M. P. 2011, *ApJ*, (arXiv1106.2796B)
- Braun, R., Oosterloo, T. A., Morganti, R., Klein, U., & Beck, R. 2007, *A&A*, 461, 455
- Briggs, D. S. 1995, *High Fidelity Deconvolution of Moderately Resolved Sources*, PhD Thesis, The New Mexico Institute of Mining and Technology, Socorro, NM
- Brisken, W. 2003, *EVLA Memo 58, Using Grasp8 to Study the VLA Beam*
- Cenacchi, E., Dallacasa, D., & Orfei, A. 2006, *Mem. S.A.It. Suppl.*, 10, 77
- Clark, B. G. 1980, *A&A*, 89, 377
- Condon, J. J. 1992, *ARA&A*, 30, 575
- Condon, J. J., Cotton, W. D., & Broderick, J. J. 2002, *AJ*, 124, 675
- Conway, J. E., Cornwell, T. J., & Wilkinson, P. N. 1990, *MNRAS*, 246, 490
- Cornwell, T. J. 2008, *IEEE J. of Selected Topics in Signal Proc.*, Vol. 2, No. 5, 793
- Cornwell, T. J., Golap, K., & Bhatnagar, S. 2008, *IEEE J. of Selected Topics in Signal Proc.*, Vol. 2, No. 5, 647
- Dumke, M., Krause, M., & Wielebinski, R., & Klein, U. 1995, *A&A*, 302, 691
- Ekers, R. D., & Sancisi, R. 1977, *A&A*, 54, 973
- Ghosh, T., et al. 2011, arXiv:1112.0509v1
- Golla, G. 1999, *A&A*, 345, 778
- Golla, G., & Hummel, E. 1994, *A&A*, 284, 777
- Heald, G. H., et al. 2009, *A&A*, 503, 409
- Heesen, V., Beck, R., Krause, M., & Dettmar, R.-J. 2011, *A&A*, 535, A79
- Hoopes, C. G., Walterbos, R. A. M., & Rand, R. J. 1999, *ApJ*, 522, 659
- Hummel, E., & Dettmar, R.-J. 1990, *A&A*, 236, 33
- Hummel, E., Lesch, H., Wielebinski, R., & Schlickeiser, R. 1988, *A&A*, 197, L29
- Hummel, E., Beck, R., & Dettmar, R.-J. 1991, *A&AS*, 87, 309
- Irwin, J. A. et al. 2011, *MNRAS*, 410, 1423
- Irwin, J. A. et al. 2012, *AJ*, Paper I
- Klein, U., Wielebinski, R., & Beck, R. 1984, *A&A*, 133, 19
- Krause, M. 2004, in *The Magnetized Interstellar Medium*, Eds. B. Uyaniker, W. Reich, and R. Wielebinski, Copernicus GmbH, Katlenburg-Lindau., 173
- Krause, M. 2009, in *Magnetic Fields in the Universe II: From Laboratory and Stars to the Primordial Universe*, *Revista Mexicana de Astronomía y Astrofísica (Serie de Conferencias)*, Eds. A. Esquivel, J. Franco, G. Garcia-Segura, E. M. de Gouveia Dal Pino, A. Lazarian, S. Lizano, & A. Raga, Vol. 36, 25
- Lee, S.-W., Irwin, J. A., Dettmar, R.-J., Cunningham, C. T., Golla, G., & Wang, Q. D. 2001, *A&A*, 377, 759

- Niklas, S., Klein, U., & Wielebinski, R. 1997, A&A, 322, 19
- Pacholczyk, A. B. 1970, Radio Astrophysics, Freeman and Co., San Francisco
- Pohl, M., & Schlickeiser, R. 1990, A&A, 239, 424
- Rand, R. J., & van der Hulst, J. M. 1993, AJ, 105, 2098
- Rau, U., & Cornwell, T. J. 2011, A&A, 532, A71
- Reich, P., Reich, W., & Testori, J. C. 2004, in The Magnetized Interstellar Medium, ed. B. Uyanikar, W. Reich, & R. Wielebinski, 63 - 68.
- Sault, R. J., & Wieringa, M. H. 1994, A&AS, 108, 585 A&A, 448, 123
- Simmons, J. F. L., & Stewart, B. G., A&A, 142, 100
- Soida, M., Krause, M., Dettmar, R.-J., & Urbanik, M. 2011, A&A, 531, 127
- Strong, A. W., Orlando, E., & Jaffe, T. R. 2011, A&A, 534, A54
- Sukumar, S., & Velusamy, T. 1985, MNRAS, 212, 367
- Vaillancourt, J. E. 2006, PASP, 118, 1340
- Wang, Q. D., et al. 1995, ApJ, 439, 176
- Wang, Q. D., Immler, S., Walterbos, R., Lauroesch, J. R., & Breitschwerdt, D. 2001, ApJ, 555, L99
- Werner, W. 1988, A&A, 201, 1

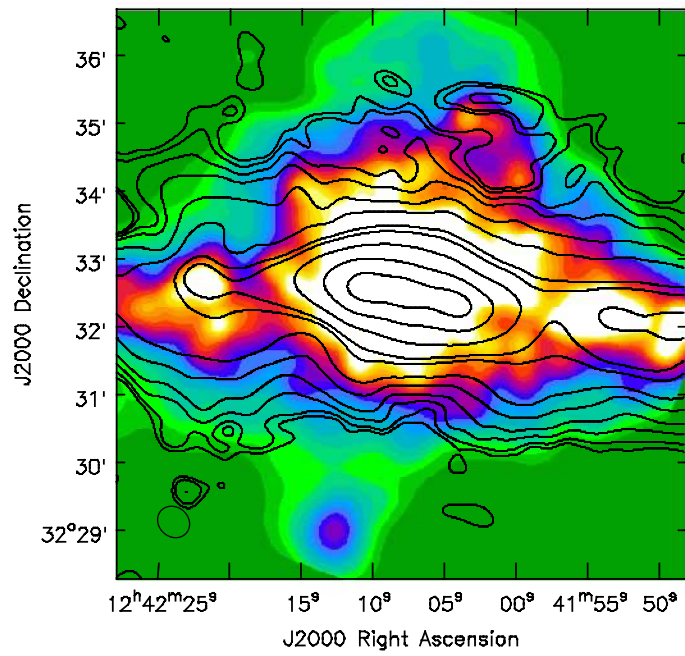


Fig. 7.— L-band contours of Fig. 1c over a colour soft X-ray image of Fig. 1a enhanced to show the X-ray - radio continuum association in the loop north of the galaxy's center.

TABLE 1
NGC 4631 OBSERVING PARAMETERS

Parameter	1.5 GHz	6.0 GHz
Array	C	C
No. antennas ^a	25	22
AC Central Frequency (GHz) ^b	1.375	5.5
BD Central Frequency (GHz) ^b	1.625	6.5
Spw bandwidth (MHz)	32	128
No. spws (AC plus BD) ^c	16	16
Total bandwidth (AC plus BD)(GHz)	0.512	2.048
No. channels/spw	64	64
Total no. channels	1024	1024
Channel separation (MHz)	0.500	2.00
Integration time (s) ^d	10	10
Obs. Time (min) ^e	30	75
Flux calibrator ^f	3C286	3C286
Zero-polarization calibrator	QQ208	QQ208
Phase calibrator	J1221+2813	J1221+2813

^aThe total number of antennas for which data were acquired during the observing session, after problem antennas were flagged.

^bAC and BD IFs are contiguous in frequency.

^cNumber of spectral windows in AC or BD IFs.

^dSingle record measurement time.

^eOn-source observing time before flagging.

^fThis source was also used as the bandpass calibrator and for determining the absolute position angle for polarization.

TABLE 2
NGC 4631 MAP PARAMETERS

Parameter	1.5 GHz			6.0 GHz		
	Briggs Rob = 0	Briggs Rob = 2	Briggs Rob = 2	Briggs Rob = 0	Briggs Rob = 2	Briggs Rob = 0
uv weighting ^a	Briggs Rob = 0	Briggs Rob = 2	Briggs Rob = 2	Briggs Rob = 0	Briggs Rob = 2	Briggs Rob = 0
uv taper (kλ) ^b	none	none	5	none	none	10
Nterms ^c	3	3	3	3	3	3
No. Self-cals ^d	1 a&p	1 a&p	1 a&p	1 a&p	1 a&p	1 a&p
	I images					
Figure label ^e	Fig. 1(a)	Fig. 1(b)	Fig. 1(c)	Fig. 2(a)	Fig. 2(b)	Fig. 2(c)
Synth. beam ^f ($''$, $''$, $^\circ$)	11.16, 10.28, -175.0	16.69, 14.77, 34.5	29.90, 26.08, 48.9	2.71, 2.63, -50.9	4.07, 3.80, 27.5	8.60, 8.52, 41.5
rms ($\mu\text{Jy beam}^{-1}$) ^g	28	45	100	4.8	5.5	8.0
	Q & U images ^h					
Synth. beam ^f ($''$, $''$, $^\circ$)	11.01, 10.13, -176.8	12.28, 14.41, 33.7	29.35, 25.51, at 48.3	2.71, 2.63, -50.8	4.07 x 3.80 at 27.5	13.15, 11.45, 27.2
rms ($\mu\text{Jy beam}^{-1}$) ^g	27	22	23	4.7	3.5	7.0

NOTE.—These parameters represent the images presented in Figs. 1 and 2.

^aSee Briggs (1995) for a description of Briggs weighting with various ‘robust’ factors.

^bScale length of Gaussian taper applied in the uv plane.

^cNumber of terms in the Taylor expansion for fitting the spectral index.

^dNumber of self-calibration iterations, where ‘a&p’ refers to amplitude and phase together.

^eMap labels, as shown in Figs. 1 and 2.

^fSynthesized beam major and minor axis and position angle.

^gRms map noise before primary beam correction.

^hThe cross-hands (RL, LR) had different sets of flags applied than the parallel hands (RR, LL), leading to differences in the synthesized beams and noise for Q and U compared to I. Cleaning also proceeded with different scales.